

Molecular dynamics study of femtosecond laser interactions with Cr targets

Eaman T. Karim, Zhibin Lin, and Leonid V. Zhigilei

Citation: *AIP Conf. Proc.* **1464**, 280 (2012); doi: 10.1063/1.4739881

View online: <http://dx.doi.org/10.1063/1.4739881>

View Table of Contents: <http://proceedings.aip.org/dbt/dbt.jsp?KEY=APCPCS&Volume=1464&Issue=1>

Published by the [American Institute of Physics](#).

Additional information on AIP Conf. Proc.

Journal Homepage: <http://proceedings.aip.org/>

Journal Information: http://proceedings.aip.org/about/about_the_proceedings

Top downloads: http://proceedings.aip.org/dbt/most_downloaded.jsp?KEY=APCPCS

Information for Authors: http://proceedings.aip.org/authors/information_for_authors

ADVERTISEMENT

**AIP**Advances

Submit Now

Explore AIP's new open-access journal

- Article-level metrics now available
- Join the conversation! Rate & comment on articles

Molecular Dynamics Study of Femtosecond Laser Interactions with Cr Targets

Eaman T. Karim^a, Zhibin Lin^b, and Leonid V. Zhigilei^a

^a *Department of Materials Science and Engineering, University of Virginia, 395 McCormick Road, Charlottesville, Virginia 22904-4745, USA*

^b *Department of Physics, Colorado School of Mines, Golden, Colorado 80401, USA*

Abstract. The mechanisms of femtosecond laser melting, spallation and ablation of a chromium target are investigated in simulations performed with a hybrid computational model that combines the classical molecular dynamics method with a continuum description of the laser excitation of conduction band electrons, electron-phonon coupling, and electron heat conduction in the irradiated target. The material response to the irradiation by a 200 fs laser pulse is studied for laser fluences covering the regimes of melting and recrystallization of the surface region of the target, photomechanical separation (spallation) of a liquid layer, and explosive disintegration and ejection of a superheated surface region. The transition from the regime of transient surface melting to the spallation is manifested by a sharp increase of the total amount of ejected material (ablation yield) and decrease in the time required for resolidification of the surface region of the target. The transition from the spallation to the phase explosion regime is characterized by a remarkable change in the composition of the ejected ablation plume (smaller droplets and larger fraction of vapor phase), increase in the time for surface resolidification, and saturation or even decrease of the total ablation yield as compared to the spallation regime. The conditions that control the transitions between the three regimes and the mechanisms of laser melting, spallation and phase explosion are established for the chromium target and related to the results of earlier simulations performed for other metals and molecular systems.

Keywords: femtosecond laser ablation, laser melting, laser spallation, molecular dynamics, two-temperature model, chromium

PACS: 61.80.Az; 79.20.Ds; 02.70.Ns; 64.70.D-; 64.70.F-; 83.60.Uv

INTRODUCTION

The fast advancement of laser technology makes ultrashort (picosecond and femtosecond) lasers increasingly accessible and expands the range of material processing applications that benefit from the rapid laser energy deposition, small heat affected zone, and minimal residual damage characteristic of the ultrashort pulse irradiation [1-4]. The ability of the ultrashort pulses to generate well-defined surface micro- and nano-structures with remarkable quality and reproducibility [5-7] and to perform high precision drilling and cutting of a broad range of materials [1-3] has been demonstrated in numerous studies.

The active expansion of the area of practical applications of ultrashort laser pulses motivates experimental and theoretical studies focused on the fundamental mechanisms of laser-materials interactions. Under conditions when laser irradiation results in permanent surface modification or material ejection (ablation), the relevant processes discussed in literature are the transient melting and resolidification of a thin surface layer [8-12], the explosive boiling (phase explosion) of a surface region

superheated beyond the limit of thermodynamic stability of the molten material [9,13-18], the melt expulsion or sputtering due to the action of ablation recoil pressure [9,19], the ejection of large droplets or fractured solid fragments caused by the relaxation of photomechanical stresses [9,20-27], as well as non-thermal phase transformations induced by the electronic excitations [28-31], photochemical reactions [32] or charge separation and Coulomb explosion [33].

Molecular dynamics (MD) simulations are playing an increasingly important role in investigations of the complex and highly non-equilibrium processes induced by short pulse laser irradiation, see recent reviews [34,35]. In particular, MD simulations of laser interactions with metal targets have provided important insights into the mechanisms and atomic-level dynamics of laser melting [9-12,25,36,37], spallation [9,24-27,38] and explosive boiling [9,17]. While most of the MD simulations of laser interactions with metals have been performed for face-centered-cubic (fcc) metals, recent simulations of laser melting and resolidification of body-centered-cubic (bcc) metal, Cr, has also been reported [11].

In this paper we report an extension of the MD simulation study of the femtosecond laser melting of Cr targets to higher fluences that cover the irradiation regimes of photomechanical spallation and explosive boiling. The results of the simulations are related to the ones obtained in a recent study of laser interactions with fcc Ni targets [9], where strong connections between the maximum melting depth, photomechanical spallation, and phase explosion are established. The computational model used in the simulations is described next, in Section 2. The results of the simulations are presented and discussed in Section 3 and summarized in Section 4.

2. COMPUTATIONAL MODEL

The simulations of laser interactions with Cr targets are performed with a combined atomistic–continuum model that couples the classical MD method with a continuum-level description of the laser excitation and subsequent relaxation of the conduction-band electrons. The model accounts for the electron heat conduction in the metal targets and provides an adequate representation of the fast heating and cooling of the surface regions of the targets. A complete description of the combined atomistic–continuum model is given in Refs. [9,24,25], whereas the parameterization for Cr is provided in Ref. [11]. Briefly, the model is based on the well-known two-temperature model (TTM) [39] that describes the time evolution of the lattice and electron temperatures, T_l and T_e , in the irradiated target by two coupled nonlinear differential equations. In the combined TTM-MD model, MD substitutes the TTM equation for the lattice temperature. The TTM equation for the electron temperature is solved by a finite difference method simultaneously with MD integration of the equations of motion of atoms. The electron temperature enters a coupling term that is added to the MD equations of motion to account for the energy exchange between the electrons and the lattice. The cells in the finite difference discretization are related to the corresponding volumes of the MD system, and the local lattice temperature is defined for each cell from the average kinetic energy of thermal motion of atoms.

The interatomic interaction in the MD part of the model is described by the embedded atom method (EAM) with the functional form and parameterization developed for Cr in Ref. [11]. The potential provides a computationally efficient yet sufficiently accurate description of real Cr. The equilibrium melting temperature, the enthalpy of melting, heat capacity, and vacancy migration energy of the EAM Cr material are within 10% of the experimental values. A good agreement of the calculated elastic properties (including the negative sign of the Cauchy pressure characteristic of Cr) with experimental data is also obtained [11].

The MD part of the TTM-MD model represents the top 100 nm surface region of the Cr target, has lateral dimensions of $8 \times 8 \text{ nm}^2$, and is composed of 630 000 atoms. Periodic boundary conditions are used in the directions parallel to the (100) free surface of the bcc crystal. To ensure non-reflecting propagation of the laser induced pressure wave from the MD part of the model, a dynamic pressure-transmitting boundary condition is applied at the bottom of MD computational cell [40,41]. The computational system is equilibrated at 300 K before applying laser irradiation.

In the continuum part of the model, beyond the MD region, the electron heat conduction and the energy exchange between the electrons and the lattice are described by the conventional TTM. The size of the continuum (TTM) region is varied between 500 nm and $1.5 \text{ }\mu\text{m}$ depending on the laser fluence and the duration of the simulation, so that no substantial changes in the electron and lattice temperatures are observed at the bottom of the continuum region by the end of the simulation.

The choice of the parameters used in the TTM equation for the electron temperature is explained in Ref. [11] and the parameters are listed below. The electronic heat capacity is $C_e = \gamma T_e$ with $\gamma = 194 \text{ Jm}^{-3}\text{K}^{-2}$, the electron-phonon coupling constant is $G = 4.2 \times 10^{17} \text{ Wm}^{-3}\text{K}^{-1}$, and the thermal conductivity is $K_e = K_0 T_e / T_l$ with $K_0 = 94 \text{ Wm}^{-1}\text{K}^{-1}$. Irradiation by a 200 fs laser pulse is represented through a source term added to the TTM equation for the electron temperature. The source term reproduces a Gaussian temporal profile and an exponential attenuation of laser intensity with the depth under the surface. An optical penetration depth of 8.9 nm at a laser wavelength of 400 nm [42] is assumed in the simulations. The reflectivity of the surface is not defined in the model since the absorbed laser fluence rather than the incident fluence is used in the discussion of the simulation results.

3. RESULT AND DISCUSSION

In this section, the threshold values of the laser fluence that correspond to the transitions between different regimes of material response to the laser irradiation are first identified from the analysis of the fluence dependence of the total ablation yield and the yield of individual (vapor-phase) atoms. The mechanisms of the fast laser melting and resolidification, the photomechanical spallation/sputtering of layer(s)/droplets of liquid material, and the phase explosion of an overheated surface region of the target are then discussed based on the results of three representative simulations performed in the corresponding irradiation regimes.

3.1 ABLATION YIELD AND COMPOSITION OF THE ABLATION PLUME

The simulations of irradiation of a bulk Cr target with a 200 fs laser pulse are performed for absorbed laser fluences ranging from 43 to 383 mJ/cm². This range of fluences covers three regimes of material response to laser irradiation: surface melting and resolidification, photomechanical spallation, and phase explosion of an overheated surface region of the target. These regimes can be identified from the fluence dependence of the total amount of material removed from the target (total ablation yield) and the number of ejected individual (vapor-phase) atoms, shown in Fig. 1.

At low laser fluences, between the thresholds for surface melting, ~50 mJ/cm² [11] and spallation, ~95 mJ/cm², the laser induced processes are limited to the melting and resolidification of a part of the surface region. The depth of the transiently melted surface region is increasing with increasing laser fluence and reaches 23 nm at the highest fluence of 85 mJ/cm² simulated in this regime. Only 3 atoms, however, are observed to evaporate from the surface of the target at this fluence.

The increase of the laser fluence above 95 mJ/cm² results in a separation of a layer of melted material from the bulk of the target, which is reflected in a step increase in the total ablation yield in Fig. 1a. As discussed in Section 3.2, the ejection of the liquid layer is driven by the relaxation of the laser-induced stresses generated in the surface region of the target under conditions of stress confinement. Therefore, by analogy with the term “spallation,” commonly used to describe the dynamic fracture that results from the reflection of a shock wave from a back surface of a sample [43,44], the material ejection due to the laser-induced stresses is called here front-surface laser spallation [26].

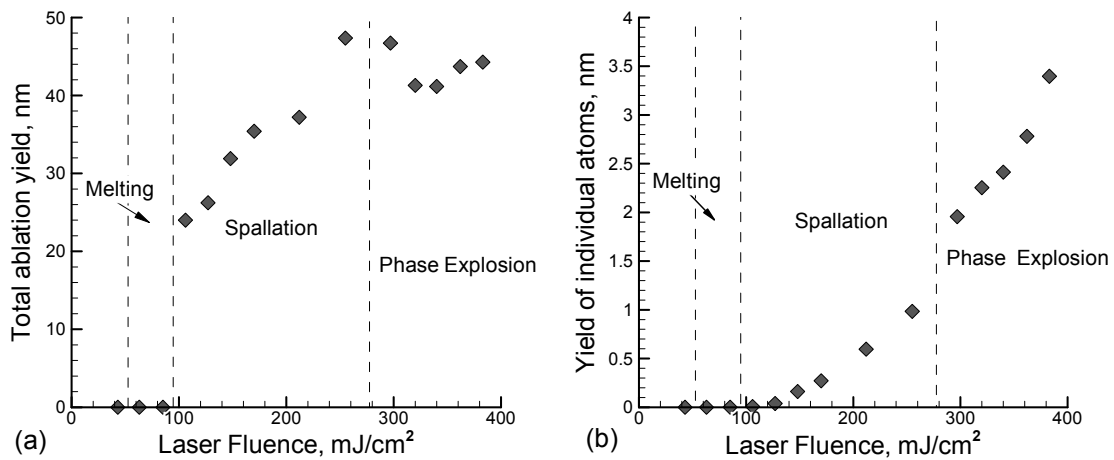


FIGURE 1. Total ablation yield (a) and number of individual atoms in the ablation plume (b) as functions of absorbed laser fluence predicted in simulations for bulk Cr targets irradiated with 200 fs laser pulses. The values of the total yield and the yield of individual atoms are expressed in units of depth in the initial target (number of ejected atoms is equivalent to the number of atoms in a layer of this depth in the initial target). The dashed lines mark the approximate values of the threshold fluences for surface melting, spallation and phase explosion.

An increase of the laser fluence above the spallation threshold results in the separation and ejection of multiple layers/droplets from the target. At the higher fluences, but still in the spallation regime, the surface layer is strongly overheated and readily disintegrates at moderate tensile stresses. The number of vapor phase atoms evaporating from the ejected liquid layers and droplets also increases with fluence but remains below 2% of the total yield, Fig. 1b.

The temperature of the surface region of the target in the spallation regime stays below the temperature required for the onset of the explosive boiling. The threshold temperature for the onset of the phase explosion can be determined in constant-pressure MD simulations of a slow heating of a metastable liquid. This approach has been used earlier to determine the threshold temperature for the onset of the explosive boiling in a system of Ar atoms [45], a molecular system represented by the breathing sphere model [46], and a Ni material simulated with EAM potential [9]. The threshold temperature for the phase explosion can be expected to be $\sim 10\%$ below the critical temperature of the material [13-15,45]. In this work, we perform a similar set of simulations for a cubic system of 6500 Cr atoms. Periodic boundary conditions are used in all directions to simulate a small region inside a bulk material. The change in volume of the system as a function of temperature, obtained in these simulations, is shown in Fig. 2. The threshold temperature for the onset of the phase explosion can be identified from a sharp increase of the volume of the system that corresponds to the explosive phase separation into liquid and vapor. This threshold temperature is found to be about 6000 K at zero pressure for the EAM Cr material.

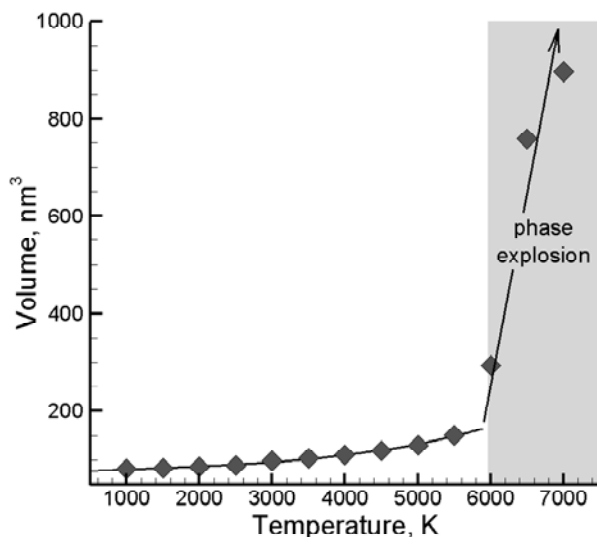


FIGURE 2. Temperature dependence of the volume of a computational cell in MD simulations of a slow constant-pressure heating of a cubic system of liquid Cr. The results of the simulations are used to determine the threshold temperature for the onset of phase explosion in the EAM Cr material.

At laser fluences that bring the surface region of the irradiated target to temperatures that reach and exceed the threshold temperature for the phase explosion, the dominant mechanism responsible for the material ejection changes from the photomechanical spallation driven by the relaxation of the laser-induced stresses to the phase explosion driven by the rapid decomposition of the overheated material into a mixture of vapor and liquid droplets. The transition to the phase explosion regime does not result in an increase in the total amount of the ejected material, Fig. 1a. Quite the reverse, the total yield decreases somewhat and saturates at fluences above the

threshold for the phase explosion. The decrease of the total yield can be explained by two factors: (1) a higher energy cost of the decomposition of the surface region of the target into a mixture of vapor and small liquid droplets as compared to the ejection of larger droplets in the spallation regime, and (2) redeposition of some of the droplets ejected at end of the ablation process back to the target due to the vapor pressure from the upper part of the plume. Indeed, deceleration and redeposition of some of the large droplets is observed in simulations performed at laser fluences of 340 mJ/cm^2 and 362 mJ/cm^2 .

The transition to the phase explosion regime is also signified by an increase in the number of vapor phase atoms in the ablation plume, Fig. 1b. Given that the total yield saturates and even decreases upon the transition to the phase explosion regime, the fraction of the vapor phase in the ablation plume increases from $\sim 2\%$ of the total yield right below the threshold for the phase explosion to $4\text{--}7\%$ above the threshold. This increase is less dramatic as compared to the one observed in the simulations performed for Ni targets [9], where the jump in the fraction of the vapor-phase atoms was from 2% to more than 10% of the total yield. The difference may be related to the material-dependent characteristics of the phase explosion process in Cr and Ni.

The increase in the fraction of the vapor-phase atoms upon the transition from the spallation to the phase explosion regime can be related to the results of plume imaging experiments [47], where the maximum ejection of nanoparticles in laser ablation of Ni targets is observed at low fluences (possible spallation), whereas the degree of the plume atomization increases at higher fluences (possible phase explosion regime). The transition from spallation to phase explosion has also been related [9] to the results of pump-probe experiments [23,48], where the observation of optical interference patterns (Newton rings) can be explained by the spallation of a thin liquid layer from the irradiated target [26,38,49] and the disappearance of the interference fringes in the central part of the laser spot [23] may be related to the transition to the phase explosion regime.

3.2 MECHANISMS OF MELTING, SPALLATION, AND PHASE EXPLOSION

The mechanisms of melting, spallation, and phase explosion are discussed in this Section based on the results of three representative simulations performed in each of these regimes. The process of melting and recrystallization is illustrated in Figs. 3 and 4 by the results of the simulation performed at an absorbed laser fluence of 85 mJ/cm^2 , about 70% above the threshold for surface melting [11].

The temporal and spatial evolution of the lattice temperature and pressure in the surface region of the target is shown in the form of contour plots in Fig. 3. The temperature plot in Fig. 3a shows that the electronic excitation by the 200 fs laser pulse and the energy transfer to the lattice due to the electron-phonon coupling result in a fast lattice heating during the first several picoseconds after the laser irradiation. The maximum temperature reached by 5.5 ps at a depth of 10 to 20 nm below the initial surface exceeds 3200 K , which is 37% above the equilibrium melting temperature of the EAM Cr material, $T_m = 2332 \text{ K}$ (this value is obtained by liquid-crystal coexistence simulations performed under constant-pressure conditions and is

slightly lower than the value of 2381 K reported earlier in Ref. [11]). At this overheating, fast homogeneous melting takes place and proceeds in a form of the fast collapse of the crystal lattice without the formation of well-defined liquid nuclei [12,25,36,37]. The fast homogeneous melting of ~ 20 nm surface region is followed by an additional slow propagation of the melting front, formed by the end of the homogeneous melting process, deeper into the target (heterogeneous melting). The transfer of the thermal energy to the latent heat of melting, cooling due to the expansion of the surface region, and the fast electronic heat conduction to the bulk of the target result in a rapid cooling of the surface region. The temperature near the liquid-crystal interface drops below the equilibrium melting temperature by the time of 50 ps and the melting turns into epitaxial recrystallization of the melted region. The velocity of the solidification front increases with increasing undercooling below the melting temperature and reaches the maximum value of about 80 m/s by the time when the melting front reaches the surface of the target and the temperature at the liquid-crystal interface drops down to about $0.8 T_m$. The values of the solidification velocity observed in the simulations are comparable to the ones estimated from pump-probe measurements performed for Ag films [8].

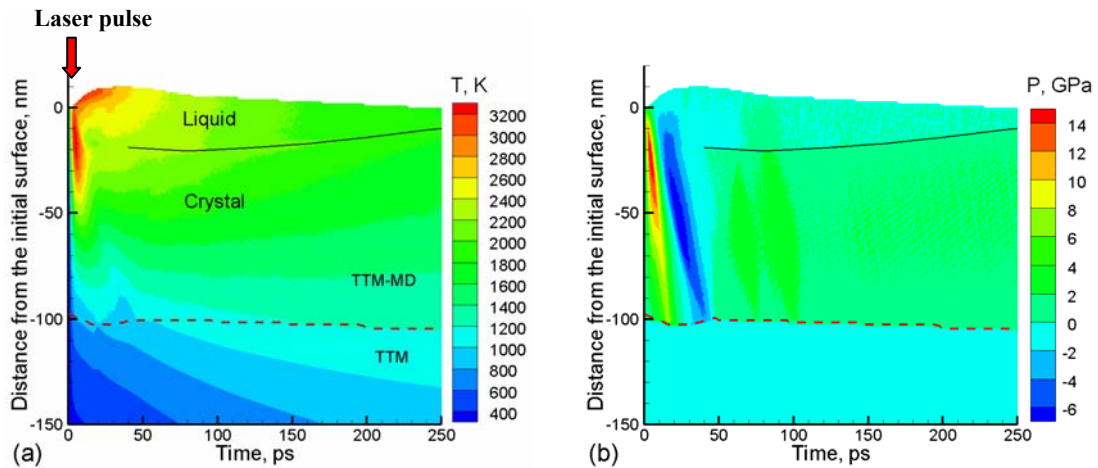


FIGURE 3. Contour plots of the spatial and temporal evolution of (a) lattice temperature and (b) pressure in a TTM-MD simulation of a bulk Cr target irradiated with a 200 fs laser pulse at an absorbed fluence of 85 mJ/cm^2 . The laser pulse is directed along the Y axes, from the top of the contour plots as shown by the red arrow. The black solid lines separate the melted and crystalline regions of the target. The red dashed lines separate the continuum (TTM) and atomistic (TTM-MD) parts of the computational system.

A visual picture of the melting and resolidification of the surface region of the target is provided by snapshots of atomic configurations shown in Fig. 4. The atoms in the snapshots are colored according to their potential energy and the red regions correspond to the melted part of the target, where the average atomic energy is elevated by the latent heat of melting. The melting process during the first 50 ps is followed by resolidification, which proceeds by the propagation of a plane solidification front towards the surface. The solidification front reaches the surface by the time of 330 ps, leaving behind a region of the target supersaturated with vacancies. The continuing shift of the system in the downward direction long after the laser pulse

(e.g., the resolidified surface is below the initial surface in the final snapshots shown in Fig. 4) is an artifact of the non-reflecting boundary condition that is not fully optimized for the potential used in the simulations. This slow downward drift of the computational cell, however, does not affect any of the results discussed in this paper.

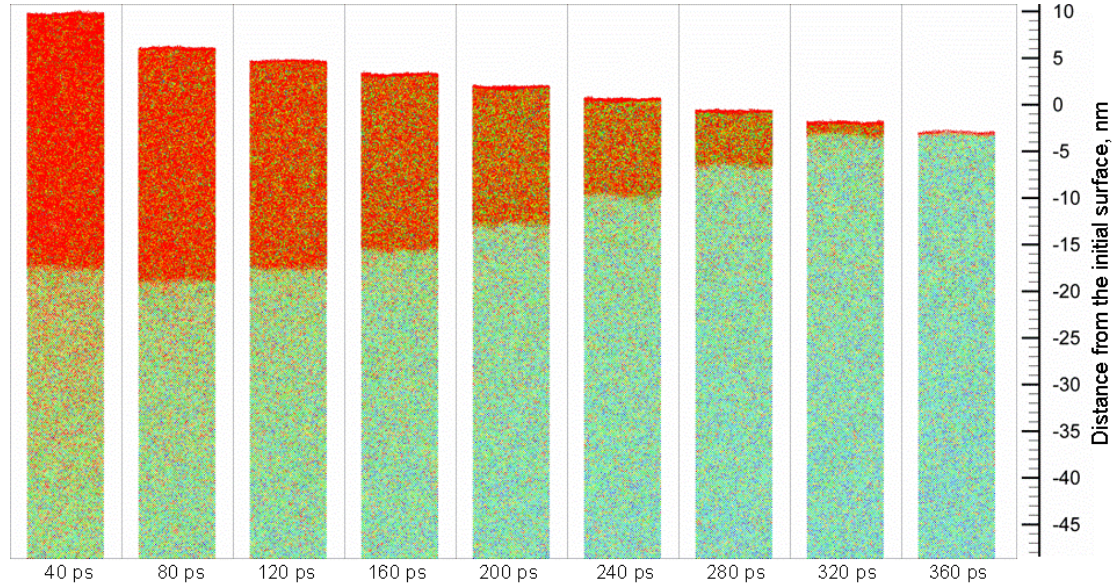


FIGURE 4. Snapshots of atomic configurations obtained in a TTM-MD simulation of a bulk Cr target irradiated with a 200 fs laser pulse at an absorbed fluence of 85 mJ/cm^2 . The snapshots are taken along the [100] view direction. The atoms are colored according to their potential energy; the red region corresponds to the elevated average atomic energy in the melted region.

The rapid increase in the lattice temperature during the first picoseconds after the laser pulse takes place under conditions of the inertial stress confinement [20,22,26] and results in the buildup of compressive stresses in the surface region of the irradiated target, Fig. 3b. The compressive stresses increase during the time of the lattice heating and reach a maximum value of $\sim 14 \text{ GPa}$ by the time of 5 ps after the laser excitation. The relaxation of the compressive stresses in the presence of the free surface of the target results in the generation of a bimodal stress wave that propagates deeper into the bulk of the target. The wave consists of a compressive component followed by a tensile one, Fig. 3b. The pressure-transmitting heat-conductive boundary condition, applied at the depth of 100 nm, ensures that both the compressive and tensile components of the pressure wave propagate without any significant reflection from the boundary separating the TTM-MD and TTM parts of the model (Fig. 3b), whereas the temperature field exhibits a seamless transition at the boundary (Fig. 3a).

The strength of the compressive and tensile stresses generated by the laser pulses increases with increasing laser fluence and, in a simulation performed at a fluence of 106 mJ/cm^2 , the tensile stresses exceed the dynamic strength of the melted material and cause spallation or separation of a melted layer from the target, Fig. 5. The microscopic mechanisms of spallation, which proceeds through the nucleation,

growth, coalescence, and percolation of multiple voids in a surface region of the target, are discussed in detail in Ref. [26]. The general characteristics of the spallation process, including the evolution of the void size distributions, appear to be common for different materials, including molecular systems [22,26,50] and metals [9,23,51]. Some of the features of the spallation process are apparent in the contour plots shown in Fig. 5. In particular, the nucleation and growth of voids is observed in the melted region of the target, at a depth that is much closer to the surface as compared with the depth where the maximum tensile stresses are generated. This is explained by the reduced ability of the overheated liquid to support transient tensile stresses generated by the laser-induced wave [26]. The spallation separates a hot surface layer from the bulk of the target and substantially accelerates the resolidification of the remaining part of the target. Indeed, the solidification front reaches the surface by 200 ps in Fig. 5 and by 330 ps in Fig. 3. A similar effect of spallation on the duration of the solidification process is also reported in Ref. [9] for Ni targets.

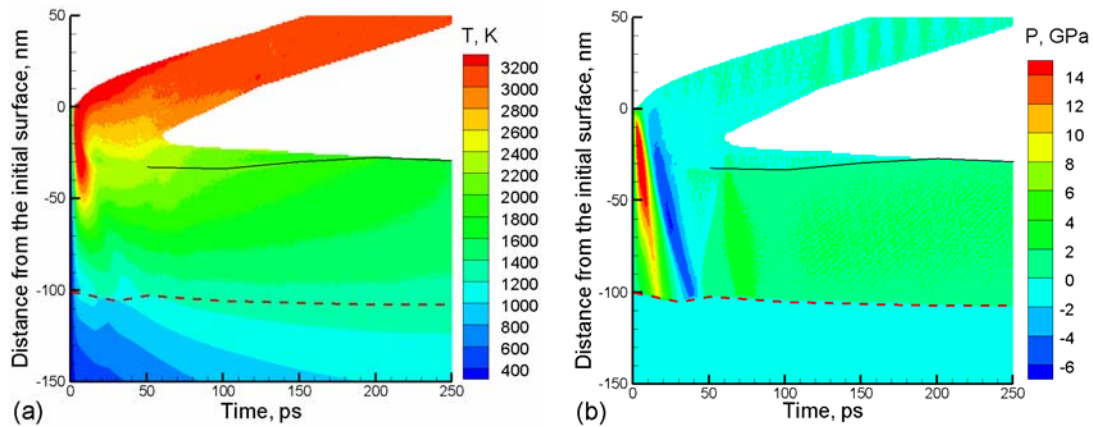


FIGURE 5. Contour plots of the spatial and temporal evolution of (a) lattice temperature and (b) pressure in a TTM-MD simulation of a bulk Cr target irradiated with a 200 fs laser pulse at an absorbed fluence of 106 mJ/cm^2 , just above the spallation threshold. The laser pulse is directed along the Y axes, from the top of the contour plots. The black solid lines separate the melted and crystalline regions of the target. The red dashed lines separate the continuum (TTM) and atomistic (TTM-MD) parts of the computational system.

Further increase of the laser fluence above the spallation threshold results in the separation and ejection of multiple layers/droplets from the target and, above $\sim 275 \text{ mJ/cm}^2$, leads to the transition from the regime of photomechanical spallation to the phase explosion characterized by a rapid decomposition of the overheated material into a mixture of vapor and liquid droplets. This transition occurs when the surface region of the irradiated target reaches and exceeds the threshold temperature for the onset of the phase explosion identified to be around 6000 K in Section 3.1, see Fig. 2. A surface region where temperature exceeds the threshold temperature for the phase explosion becomes unstable and disintegrates in an explosive manner. An example illustrating this ablation mechanism is shown in Fig. 6, where the temperature and pressure contour plots are shown for a simulation performed at an absorbed fluence of 298 mJ/cm^2 .

The transition to the regime of phase explosion not only alters the composition of the ejected plume (increases the fraction of the vapor phase, Fig. 1), but also changes the dynamics of the ablation plume expansion and its interaction with the target. The vapor pressure released in the explosive decomposition of the top part of the target slows down the expansion of lower part of the ejected plume and prolongs its interaction with the new surface of the target. This interaction slows down the cooling of the surface and significantly increases the time scales of the melting and resolidification processes, compare Figs. 5 and 6. The transition from the spallation to the phase explosion regime also affects the characteristics of the pressure wave generated by the laser irradiation, Fig. 6b. While the compressive component of the pressure wave continues to increase linearly with increasing laser fluence, the tensile component starts to decrease in the spallation and phase explosion regimes. This decrease can be attributed to the reduced ability of the strongly overheated part of the target to support the transient tensile stresses, as well as to the compressive ablation recoil pressure that partially cancels the tensile component of the wave.

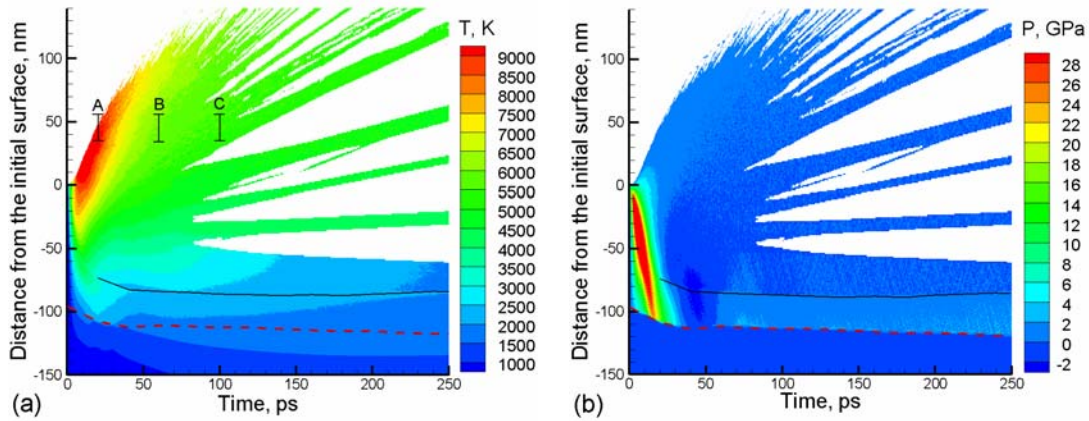


FIGURE 6. Contour plots of the spatial and temporal evolution of (a) lattice temperature and (b) pressure in a TTM-MD simulation of a bulk Cr target irradiated with a 200 fs laser pulse at an absorbed fluence of 298 mJ/cm^2 , just above the threshold for the phase explosion. The laser pulse is directed along the Y axes, from the top of the contour plots. The black solid lines separate the melted and crystalline regions of the target. The red dashed lines separate the continuum (TTM) and atomistic (TTM-MD) parts of the computational system. Marks A, B, and C show the time and locations in the ablation plume for which snapshots of atomic configurations are shown in Fig. 7.

The illustrate the process of the decomposition of the overheated material in the regime of phase explosion, snapshots of the ablation plume, taken at the same height above the initial surface, are shown in Fig. 7 for different times marked in the contour plot in Fig. 6a. The first snapshot, shown for 20 ps in Fig. 7a, provides an atomic-level picture of the homogeneous expansion of the strongly overheated top layer of the target. The homogeneous expansion is followed by the appearance and growth of density fluctuations and formation of a foamy transient structure of interconnected liquid regions surrounded by vapor-phase atoms, Fig. 7b. The foamy transient structure subsequently decomposes into separate elongated liquid droplets, Fig. 7c, which gradually develop into spherical droplets in a process driven by the minimization of surface energy of the droplets.

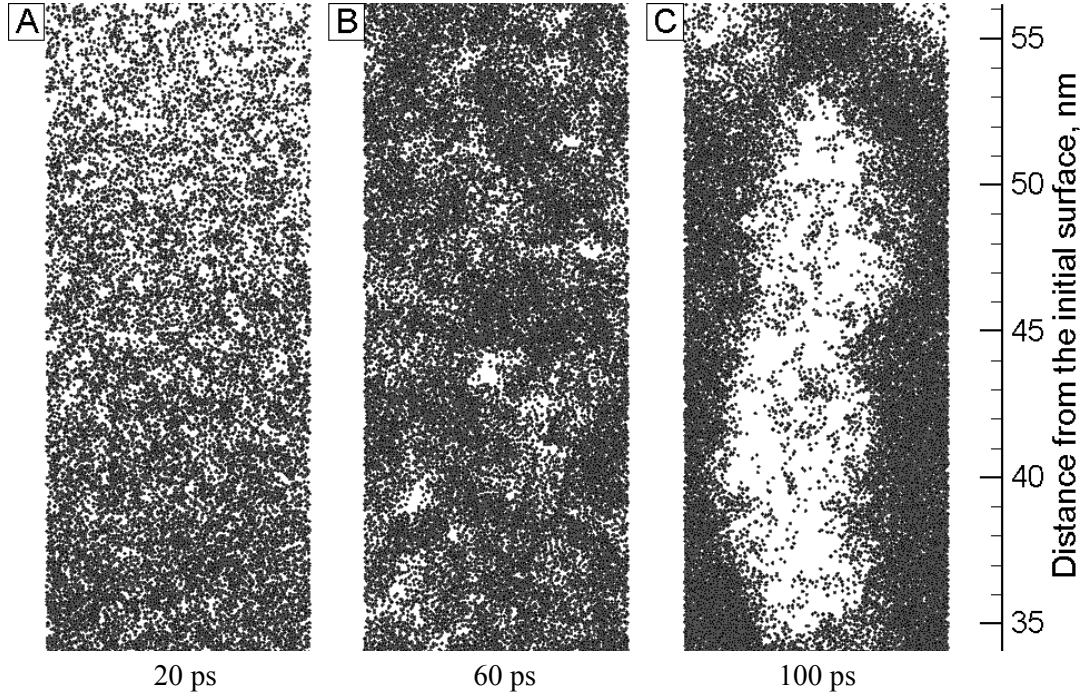


FIGURE 7. Snapshots of atomic configurations obtained in a TTM-MD simulation of a bulk Cr target irradiated with a 200 fs laser pulse at an absorbed fluence of 298 mJ/cm^2 , close to the threshold for the phase explosion. Snapshots are taken at times and locations marked in the temperature contour plot in Fig. 6a. The snapshots are taken along the [010] view direction.

The dynamics of the material ejection and the composition of the ablation plume predicted in the simulations performed in the phase explosion regime are affected by the conditions of the stress confinement created by the fast laser energy deposition. The phase explosion occurring under conditions of stress confinement takes place simultaneously with the relaxation of the laser-induced stresses, resulting in a more vigorous material ejection, higher ablation yields, and smaller fraction of the vapor phase as compared to the “pure” phase explosion, characteristic for longer pulses. A similar effect of the stress confinement has been observed earlier in MD simulations of laser ablation Ni targets [9] and molecular systems [16,22], where a higher ablation yields, larger droplets, smaller fractions of the vapor phase, and higher ejection velocities are observed in simulations performed for irradiation conditions that correspond to the stress confinement. A relatively weak phase explosion, on the other hand, has been reported in MD simulations of nanosecond laser ablation of a Lennard-Jones system [52], where vapor phase molecules are found to account for the largest fraction of the ablation yield.

4. SUMMARY

A series of simulations of femtosecond laser interactions with Cr targets is performed with a hybrid computational model that combines the atomistic MD method with the continuum TTM model. The results of the simulations reveal the microscopic mechanisms of laser-induced melting and recrystallization of the surface region of the

target, photomechanical spallation, and explosive disintegration and ejection of a superheated surface region. The physical conditions that result in the transitions from the melting regime to spallation and from spallation to the regime of phase explosion are discussed based on the results of the simulations. The ejection of the liquid layers and large droplets in the spallation regime are found to provide an energetically-efficient way to remove material from the irradiated target. The transition from the spallation to the phase explosion regime, on the other hand, reduces the ablation efficiency and is characterized by a remarkable change in the composition of the ablation plume (smaller droplets and larger fraction of vapor phase). The timescale of melting and resolidification are also affected by the dominant mechanism of the material ejection: the onset of spallation interrupts the heat conduction from the hot surface layer separated from the bulk the target, leading to a sharp drop in the maximum melting depth and the duration of the melting process, whereas the transition to the phase explosion regime increases the melting depth and the duration of the melting and resolidification cycle due to the continued interaction of the ablation plume with the surface of the target. The predictions of the simulations are related to the experimental observations and the results of earlier MD simulations of laser interactions with other metal targets and molecular systems.

ACKNOWLEDGMENTS

Financial support for this work is provided by the National Science Foundation (NSF) through Grant No. DMR-0907247. Computational support is provided by NCCS at ORNL (project MAT009) and NSF through TeraGrid resources (project TG-DMR110090).

REFERENCES

1. B. N. Chichkov, C. Momma, S. Nolte, F. von Alvensleben, and A. Tünnermann, *Appl. Phys. A: Mater. Sci. Process.* **63**, 109-115 (1996).
2. R. L. Harzic, N. Huot, E. Audouard, C. Jonin, and P. Laporte, *Appl. Phys. Lett.* **80**, 3886-3888 (2002).
3. S.-S. Wellershoff, J. Hohlfeld, J. Güdde, and E. Matthias, *Appl. Phys. A: Mater. Sci. Process.* **69**, S99-S107 (1999).
4. V. Margetic, K. Niemax, and R. Hergenröder, *Anal. Chem.* **75**, 3435-3439 (2003).
5. A. I. Kuznetsov, J. Koch, and B. N. Chichkov, *Appl. Phys. A: Mater. Sci. Process.* **94**, 221-230 (2009).
6. D. Hwang, S.-G. Ryu, N. Misra, H. Jeon, and C. P. Grigoropoulos, *Appl. Phys. A: Mater. Sci. Process.* **96**, 289-306 (2009).
7. R. R. Gattass and E. Mazur, *Nature Photonics* **2**, 219-225 (2008).
8. W. L. Chan, R. S. Averback, D. G. Cahill, and Y. Ashkenazy, *Phys. Rev. Lett.* **102**, 095701 (2009).
9. L. V. Zhigilei, Z. Lin, and D. S. Ivanov, *J. Phys. Chem. C* **113**, 11892-11906 (2009).

10. C. Wu, D. A. Thomas, Z. Lin, and L. V. Zhigilei, *Appl. Phys. A: Mater. Sci. Process.* **104**, 781-792 (2011).
11. Z. Lin, R. A. Johnson, and L. V. Zhigilei, *Phys. Rev. B* **77**, 214108 (2008).
12. D. S. Ivanov and L. V. Zhigilei, *Phys. Rev. Lett.* **98**, 195701 (2007).
13. M. M. Martynyuk, *Sov. Phys. Tech. Phys.* **21**, 430-433 (1976).
14. A. Miotello and R. Kelly, *Appl. Phys. A: Mater. Sci. Process.* **69**, S67-S73 (1999).
15. N. M. Bulgakova and A. V. Bulgakov, *Appl. Phys. A: Mater. Sci. Process.* **73**, 199-208 (2001).
16. L. V. Zhigilei, *Appl. Phys. A: Mater. Sci. Process.* **76**, 339-350 (2003).
17. C. Cheng and X. Xu, *Phys. Rev. B* **72**, 165415 (2005).
18. M. E. Povarnitsyn, T. E. Itina, M. Sentis, K. V. Khishchenko, and P. R. Levashov, *Phys. Rev. B* **75**, 235414 (2007).
19. V. V. Semak, J. G. Thomas, and B. R. Campbell, *J. Phys. D: Appl. Phys.* **37**, 2925-2931 (2004).
20. G. Paltauf and P. E. Dyer, *Chem. Rev.* **103**, 487-518 (2003).
21. J. Yang, Y. Zhao, N. Zhang, Y. Liang, and M. Wang, *Phys. Rev. B* **76**, 165430 (2007).
22. L. V. Zhigilei and B. J. Garrison, *J. Appl. Phys.* **88**, 1281-1298 (2000).
23. M. B. Agranat, S. I. Anisimov, S. I. Ashitkov, V. V. Zhakhovskii, N. A. Inogamov, K. Nishihara, Yu. V. Petrov, V. E. Fortov, and V. A. Khokhlov, *Appl. Surf. Sci.* **253**, 6276-6282 (2007).
24. C. Schäfer, H. M. Urbassek, and L. V. Zhigilei, *Phys. Rev. B* **66**, 115404 (2002).
25. D. S. Ivanov and L. V. Zhigilei, *Phys. Rev. B* **68**, 064114 (2003).
26. E. Leveugle, D. S. Ivanov, and L. V. Zhigilei, *Appl. Phys. A: Mater. Sci. Process.* **79**, 1643-1655 (2004).
27. B. J. Demaske, V. V. Zhakhovsky, N. A. Inogamov, and I. I. Oleynik, *Phys. Rev. B* **82**, 064113 (2010).
28. K. Sokolowski-Tinten, J. Bialkowski, M. Boing, A. Cavalleri, and D. von der Linde, *Phys. Rev. B* **58**, R11805-R11808 (1998).
29. A. M. Lindenberg, S. Engemann, K. J. Gaffney, K. Sokolowski-Tinten, J. Larsson, P. B. Hillyard, D. A. Reis, D. M. Fritz, J. Arthur, R. A. Akre, M. J. George, A. Deb, P. H. Bucksbaum, J. Hajdu, D. A. Meyer, M. Nicoul, C. Blome, Th. Tschentscher, A. L. Cavalieri, R.W. Falcone, S. H. Lee, R. Pahl, J. Rudati, P. H. Fuoss, A. J. Nelson, P. Krejčík, D. P. Siddons, P. Lorazo, and J. B. Hastings, *Phys. Rev. Lett.* **100**, 135502 (2008).
30. V. Recoules, J. Clérrouin, G. Zérah, P. M. Anglade, and S. Mazevet, *Phys. Rev. Lett.* **96**, 055503 (2006).
31. H. O. Jeschke and M. E. Garcia, "Ultrafast structural changes induced by femtosecond laser pulses," Chapter 7 in *Nonlinear Optics, Quantum Optics, and Ultrafast Phenomena with X-Rays*, ed. B. W. Adams (Springer-Verlag, New York, 2003), pp. 175-214.
32. H. Masuhara, T. Asahi, and Y. Hosokawa, *Pure Appl. Chem.* **78**, 2205-2226 (2006).
33. N. M. Bulgakova, R. Stoian, A. Rosenfeld, I. V. Hertel, W. Marine, and E. E. B. Campbell, *Appl. Phys. A: Mater. Sci. Process.* **81**, 345-356 (2005).
34. L. V. Zhigilei, Z. Lin, D. S. Ivanov, E. Leveugle, W. H. Duff, D. Thomas, C. Sevilla, and S. J. Guy, "Atomic/molecular-level simulations of laser-materials interactions," Chapter 3 in *Laser-Surface Interactions for New Materials Production: Tailoring Structure and Properties*, Springer Series in Materials Science, Vol. **130**, Edited by A. Miotello and P. M. Ossi (Springer Verlag: New York, 2010), pp. 43-79.

35. L. V. Zhigilei, E. Leveugle, D. S. Ivanov, Z. Lin, and A. N. Volkov, "Molecular dynamics simulations of short pulse laser ablation: Mechanisms of material ejection and particle generation," Chapter 7 in *Nanosized Material Synthesis by Action of High-Power Energy Fluxes on Matter* (Siberian Branch of the Russian Academy of Sciences: Novosibirsk, 2010), pp. 147-220, in Russian.
36. Z. Lin and L. V. Zhigilei, *Phys. Rev. B* **73**, 184113 (2006).
37. Z. Lin, E. M. Bringa, E. Leveugle, and L. V. Zhigilei, *J. Phys. Chem. C* **114**, 5686-5699 (2010).
38. S. I. Anisimov, V. V. Zhakhovskii, N. A. Inogamov, K. Nishihara, A. M. Oparin, and Yu. V. Petrov, *JETP Lett.* **77**, 606-610 (2003).
39. S. I. Anisimov, B. L. Kapeliovich, and T. L. Perel'man, *Sov. Phys. JETP* **39**, 375-377 (1974).
40. L. V. Zhigilei and B. J. Garrison, *Mat. Res. Soc. Symp. Proc.* **538**, 491-496 (1999).
41. C. Schafer, H. M. Urbassek, L. V. Zhigilei, and B. J. Garrison, *Comp. Mater. Sci.* **24**, 421-429 (2002).
42. *Handbook of Optical Constants of Solids I/II*, edited by D. Palik (Academic Press, London, 1985/1991).
43. V. E. Fortov, V. V. Kostin, and S. Eliezer, *J. Appl. Phys.* **70**, 4524-4531 (1991).
44. H. Tamura, T. Kohama, K. Kondo, and M. Yoshida, *J. Appl. Phys.* **89**, 3520-3522 (2001).
45. B. J. Garrison, T. E. Itina, and L. V. Zhigilei, *Phys. Rev. E* **68**, 041501 (2003).
46. E. Leveugle and L. V. Zhigilei, *J. Appl. Phys.* **102**, 074914 (2007).
47. S. Amoruso, R. Bruzzese, C. Pagano, and X. Wang, *Appl. Phys. A: Mater. Sci. Process.* **89**, 1017-1024 (2007).
48. K. Sokolowski-Tinten, J. Bialkowski, A. Cavalleri, D. von der Linde, A. Oparin, J. Meyer-ter-Vehn, and S. I. Anisimov, *Phys. Rev. Lett.* **81**, 224-227 (1998).
49. N. A. Inogamov, Y. V. Petrov, S. I. Anisimov, A. M. Oparin, N. V. Shaposhnikov, D. von der Linde, and J. Meyer-ter-Vehn, *JETP Lett.* **69**, 310-316 (1999).
50. A. G. Zhidkov, L. V. Zhigilei, A. Sasaki, and T. Tajima, *Appl. Phys. A: Mater. Sci. Process.* **73**, 741-747 (2001).
51. L. V. Zhigilei, D. S. Ivanov, E. Leveugle, B. Sadigh, and E. M. Bringa, *High-Power Laser Ablation V*, edited by C. R. Phipps, *Proc. SPIE* **5448**, 505-519 (2004).
52. L. Zhang and X. Wang, *Appl. Surf. Sci.* **255**, 3097-3103 (2008).